


Article

First-Principles Investigation of Atomic Hydrogen Adsorption and Diffusion on/into Mo-doped Nb (100) Surface

Yang Wu ¹, Zhongmin Wang ^{1,2,*}, Dianhui Wang ^{1,*} , Jiayao Qin ¹, Zhenzhen Wan ¹, Yan Zhong ^{1,2}, Chaohao Hu ^{1,2,*} and Huaiying Zhou ^{1,2}

¹ School of Materials Science and Engineering, Guilin University of Electronic Technology, Guilin 541004, China; wuyang@ihep.ac.cn (Y.W.); qjyhs2012@163.com (J.Q.); qingfeng521567@163.com (Z.W.); zyguet@163.com (Y.Z.); zhy@guet.edu.cn (H.Z.)

² Guangxi Key Laboratory of Information Materials, Guilin University of Electronic Technology, Guilin 541004, China

* Correspondence: zmwang@guet.edu.cn (Z.W.); devix@mails.guet.edu.cn (D.W.); chaohao.hu@guet.edu.cn (C.H.); Tel.: +86-139-7831-6492 (Z.W.); +86-150-0773-1239 (D.W.); +86-137-6843-4525 (C.H.)

Received: 6 November 2018; Accepted: 28 November 2018; Published: 3 December 2018



Abstract: To investigate Mo doping effects on the hydrogen permeation performance of Nb membranes, we study the most likely process of atomic hydrogen adsorption and diffusion on/into Mo-doped Nb (100) surface/subsurface (in the Nb₁₂Mo₄ case) via first-principles calculations. Our results reveal that the (100) surface is the most stable Mo-doped Nb surface with the smallest surface energy (2.75 J/m²). Hollow sites (HSs) in the Mo-doped Nb (100) surface are H-adsorption-favorable mainly due to their large adsorption energy (−4.27 eV), and the H-diffusion path should preferentially be HS→TIS (tetrahedral interstitial site) over HS→OIS (octahedral interstitial site) because of the correspondingly lower H-diffusion energy barrier. With respect to a pure Nb (100) surface, the Mo-doped Nb (100) surface has a smaller energy barrier along the HS→TIS pathway (0.31 eV).

Keywords: Nb (100) surface; Mo doping; H adsorption; H diffusion; first-principles calculation

1. Introduction

The interaction between hydrogen and metal surfaces is an interesting topic in science and engineering, and has been investigated by both experimental [1–3] and theoretical [4,5] approaches. Over 80 percent of synthetic chemicals are produced with the application of catalysts, meaning that the interactions of hydrogen with catalytic metal surfaces during heterogeneous catalysis are of great interest for several important processes [6–8] including petrochemical processing, pharmaceutical production [9], highly efficient electrocatalysis [10], fine chemical production [11], and conversion of biomass to fuels and chemicals [12]. Meanwhile, hydrogen–metal interactions have attracted further attention due to the central role of hydrogen as a clean and efficient energy source [13,14]. With the increasing demand for high purity hydrogen in the fields of fuel cell, new materials for hydrogen separation/purification are being explored. Consequently, the study of the behavior of both absorbed and adsorbed hydrogen on/into the metal surface/subsurface is important for achieving a deep understanding of the hydrogen-permeation properties of such metallic membranes [15,16].

Considerable experimental and theoretical studies of the hydrogen sorption on many single-crystal metal surfaces have been carried out. For example, Ferrin et al. [4,15] performed a comprehensive theoretical study addressing adsorption and absorption energies and subsurface penetration barriers

of hydrogen on different low-index surface terminations of 17 transition metals (TM) by first-principles calculations. Lauhon et al. further studied the diffusion of atomic hydrogen on Cu (001) via scanning tunneling microscope (STM) measurements. The diffusion of H atoms was measured as a function of temperature, and a transition from thermally activated diffusion to quantum tunneling was observed at 60 K [16]. Recently, Gómez et al. reported an extensive study of adsorption and diffusion of hydrogen atoms on the (100) surfaces of fcc Au, Cu, Ag, and Pt, performed by means of density functional theory (DFT) calculations [17,18]. Based on elucidating the preferential adsorption sites of hydrogen on each metal, they calculated the adsorption distances and energies of atomic hydrogen at the top, hollow, and bridge sites of the (100) surfaces. The numerous studies focused on this topic have proved the importance of understanding the mechanism of hydrogen–metal-surface-related phenomena.

Pd and its alloys are excellent materials for hydrogen separation and purification, but their high cost and scarcity should be noted. Currently, niobium (Nb), a Group VB (e.g., V, Nb, Ta, etc.) TM, has attracted much attention as one of the most promising hydrogen separation materials due to its relatively low price [3], excellent high-temperature mechanical properties, and corrosion resistance [19–21]. However, Nb often exhibit poor resistance to hydrogen embrittlement and therefore is limited in the practical application [22–25]. Experimental and theoretical studies have verified that alloying Nb with other metals is an effective approach to solve this problem [26–30]. Hu et al. [31] reported that the W doping is supposed to be the key role in enhancing the mechanical properties of Nb₁₆H, and is not conducive to the structural stability of the Nb₁₅WH (TIS) phase. Moreover, doping Nb with W can reduce the diffusion barrier of H, and enhance diffusion paths for H [32].

Both W and Mo are high-Z refractory metals (i.e., refractory metals containing impurities with high atomic numbers (Z) with similar physical properties. Comparing with W, Mo has a lower melting point (2883 K) and a lower erosion rate. Moreover, H has higher diffusivity and lower solubility in Mo, leading to lower H retention [33–35]. These characteristics make Mo an important alloying candidate of Nb-based membranes for hydrogen permeation.

To gain a detailed understanding of the hydrogen-permeation behavior of Mo-doped Nb membranes, adsorption and diffusion of hydrogen atoms on a Mo-doped Nb (Nb₁₂Mo₄) surface have been investigated by first-principles calculations in this work. Furthermore, we discuss the most favorable process of H adsorption and diffusion on/into a Mo-doped Nb (100) surface/subsurface. We believe this work is important to comprehensively understand the basic mechanism of atomic hydrogen sorption on TM surfaces and the influence of element doping, and contribute to the design of Nb-based alloys for H-storage and H-separation applications.

2. Computational Details

Our calculations were carried out with the use of the Vienna Ab-initio Simulation Package (VASP) [36,37]. The interactions between the core and valence electrons were described with the projector augmented wave (PAW) approach [38,39]. Exchange correlation functions were generalized gradient approximations (GGA) developed by Perdew et al. [40]. An energy cutoff of 360 eV was used for the plane-wave basis sets, and a grid with $2\pi \times 0.03 \text{ \AA}^{-1}$ resolution in the Brillouin zone was used for all calculations to minimize the error from the k -point meshes. During structure relaxation, the lattice parameters, volume, and atomic positions were fully optimized with in-symmetry restrictions until the total energy converged to 10^{-5} eV in the self-consistent loop. Relaxed until the maximum force on each atom was less than 0.01 eV/\AA . The electrons of the Nb $4d^45s^1$ and the Mo $4d^55s^1$ orbitals were treated as valence electrons. To study the diffusion properties of atomic hydrogen from the surface into the subsurface of Mo-doped Nb (100), we used the climbing image nudged elastic band (CI-NEB) method [41] to determine the diffusion barriers between the initial and final positions.

3. Results and Discussion

3.1. Surface Model of Mo-doped Nb

In $\text{Nb}_{16-x}\text{Mo}_x\text{H}$ system, $\text{Nb}_{12}\text{Mo}_4\text{H}$ has the highest absolute value of ΔH_f , which is favorable for dehydrogenation. Therefore, $\text{Nb}_{12}\text{Mo}_4\text{H}$ was selected to build the slab model for further study, which is depicted in Figure 1a. There are two high symmetrical interstitial sites in the region between the first and second atomic layer, which are tetrahedral interstitial site (TIS) and octahedral interstitial site (OIS), as shown in Figures 1b and 1c. Due to the similar atomic radius of Mo compared to Nb, the crystal keeps the cubic structure after Mo-doping. The equilibrium lattice constant (3.304 Å) of bulk Nb agrees well with experimental values (3.305 Å) [42]. For the (100) surface, we built a slab model with seven atomic layers, which is depicted in Figure 1d.

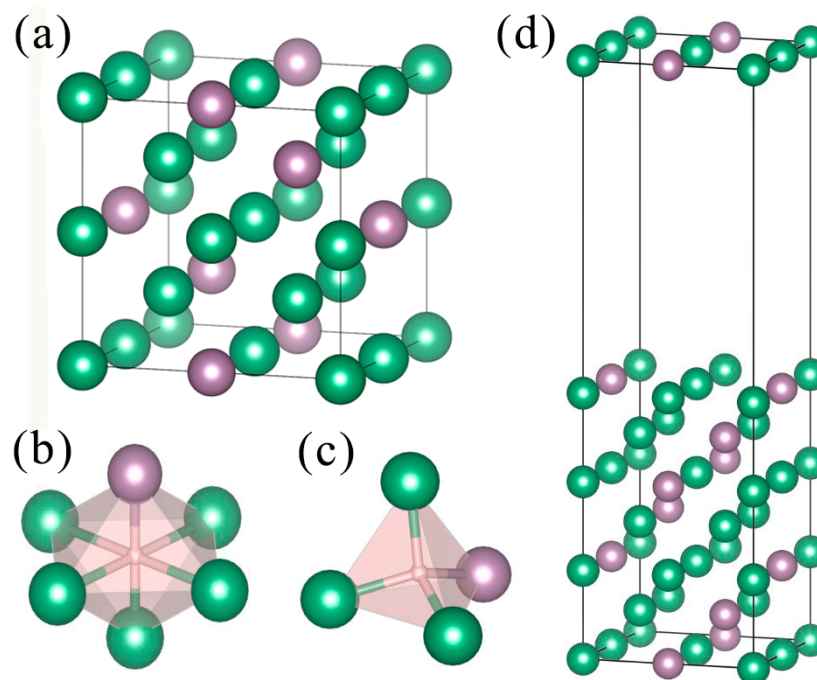


Figure 1. Theoretical models of $\text{Nb}_{12}\text{Mo}_4$ used in the calculations: (a) bulk model; (b) an octahedral interstitial site (OIS), (c) a tetrahedral interstitial site (TIS); (d) slab model. Nb atoms are represented by green spheres, and Mo atoms are represented by gray spheres.

Surface energy is an important parameter of a metal surface that can be utilized to explain the physical and chemical processes and surface stability. Cutting surfaces from bulk crystal breaking various chemical bonds, which increases the energy of the system, thereby resulting in instability of the surface systems. The surface energy is defined as [14]

$$\sigma = (E_{\text{slab}} - n \times E_{\text{bulk}}) / (2A) \quad (1)$$

Here, E_{slab} , E_{bulk} , n , and A represent the total energy of the slab, the total energy of the corresponding bulk material, the number of atoms contained in the slab and the area of the surface, respectively. In the structure optimization calculations, the atoms in the top three layers were fully relaxed, and the atoms in the other layers were fixed at their bulk positions. Table 1 lists the calculated surface energies of slab models with different numbers of atomic layers. The surface energy of pure Nb (100) surface is also calculated for comparison. The results agree well with the values from Baskes et al. [43]. The surface energy of $\text{Nb}_{12}\text{Mo}_4(100)$ surface and $\text{Nb}_{12}\text{Mo}_4(111)$ surface tend to be stable when there are more than five atomic layers. Moreover, the $\text{Nb}_{12}\text{Mo}_4(100)$ surface is the most

stable one with the smallest surface energy (2.75 J/m²). Therefore, we select Nb₁₂Mo₄(100) surface for further study.

Table 1. Calculated surface energies of pure Nb (100), Nb₁₂Mo₄ (100) and (111) for of different numbers of atomic layers. Experimental value [43] is listed for comparison.

	Surface Energies (eV)						
	4 Layers	5 Layers	6 Layers	7 Layers	8 Layers	9 Layers	10 Layers
Pure Nb (100)	2.63	2.45	2.43	2.42	2.44	2.44	2.44
Pure Nb (100) ^a		2.3–2.7					
Nb ₁₂ Mo ₄ (100)	2.72	2.73	2.74	2.75	2.75	2.75	2.75
Nb ₁₂ Mo ₄ (111)	3.28	3.31	3.32	3.32	3.32	3.32	3.32

^a Ref. [43].

To determine a practicable number of atomic layers and the vacuum region of Mo-doped Nb (100) surface model, we calculate the changes of the interlayer distances during structure relaxation as the following relationship [44,45]

$$\Delta d_{i-j} = d_{i-j} - d_0 \quad (2)$$

Here, d_0 denotes the layer distance between the i - and j -layers of the unrelaxed slab model established from a geometry-optimized bulk model and d_{i-j} denotes the corresponding layer distance of the optimized slab model. From the calculated results depicted in Figure 2, we can infer that the interlayer distance between the outermost layer and secondary outer layer tends to be stable when there are more than six atomic layers. According to the previously calculated surface energies, seven atomic layers are sufficient to avoid the effects of external forces in z -axis.

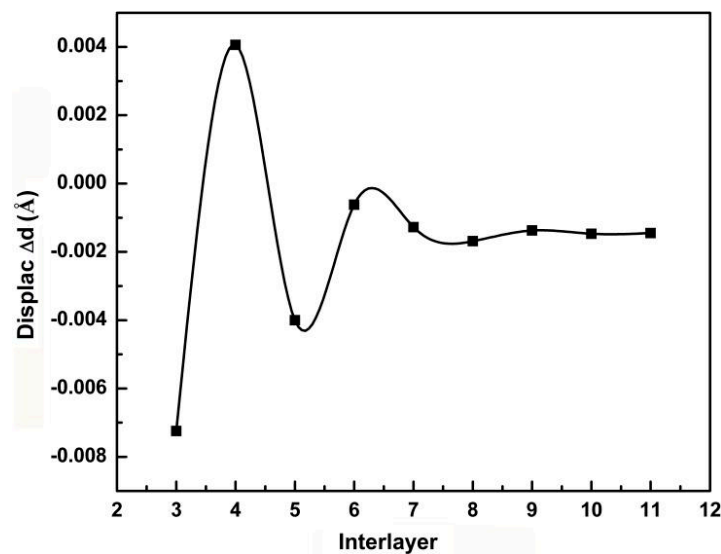


Figure 2. Change in interlayer distance as function of interlayer number in Nb (100) surface model.

In addition, to ensure that hydrogen permeation process is not influenced by periodicity, a vacuum region between the atomic layers in the (100) surface is required. Thus, the work function of (100) surface model with seven atomic layers and a 12 Å vacuum layer along the surface normal direction (z -axis) is calculated, and is depicted in Figure 3. The flat line in the figure indicating that the work function converges in the vacuum region. Therefore, we employed a slab model of seven atomic layers with a 12 Å vacuum layer of (100) surface for further hydrogen permeation analysis.

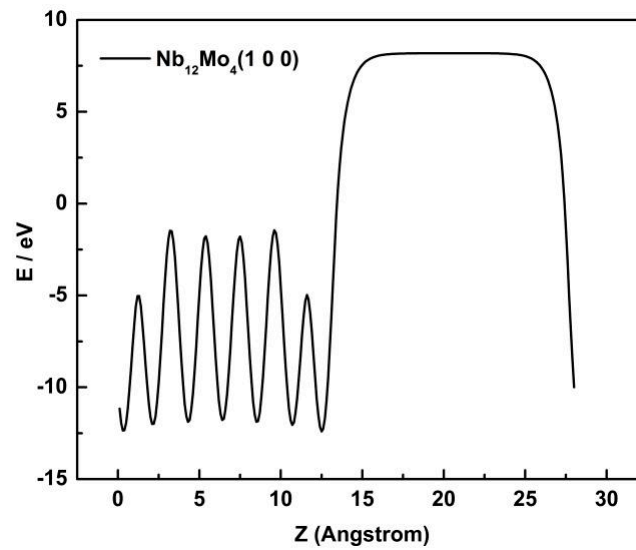


Figure 3. Work function along surface normal direction (Z -axis) for $\text{Nb}_{12}\text{Mo}_4$ (100) surface model with seven atomic layers.

3.2. H Atom Adsorption Sites of Mo-doped Nb (100) Surface

Based on the slab model of Mo-doped Nb (100) surface, there are three possible adsorption sites for hydrogen atoms, i.e., top site (TS), bridge site (BS), and hollow site (HS), as shown in Figure 4. The adsorption energies (E_{ads}) are calculated to characterize the preferred location of the adsorbed hydrogen atom. When Nb doping is considered, E_{ads} can be expressed as

$$E_{ads} = E(\text{Nb}_n\text{Mo}_{m-n}\text{H}) - E(\text{Nb}_n\text{Mo}_{m-n}) - E(\text{H}) \quad (3)$$

Here, m represents the total number of atoms, n represents the number of Nb atoms in the slab model, $E(\text{H}) = -0.019$ eV, $E(\text{Nb}_n\text{Mo}_{m-n})$ and $E(\text{Nb}_n\text{Mo}_{m-n}\text{H})$ the total energies of the corresponding crystal structures. The calculated E_{ads} values are summarized in Table 2. Among the possible positions, the largest adsorption energy (-4.27 eV) belongs to the hollow site on top of Nb atom (H1), which indicates that H1 sites are the preferential sites of adsorbed hydrogen atoms. In addition, the average vertical distance between adsorbed H atom and the top layer ($d_{\text{H-Surf}}$) as well as the distance between H atom and TM atoms ($d_{\text{H-TM}}$) are also calculated and listed in Table 2. The bonding lengths ($d_{\text{H-TM}}$) between the hydrogen-atom and TM atom show the descending on the hollow, bridge and top sites, respectively. The smallest $d_{\text{H-Surf}}$ (0.44 Å) belongs to the H1 site, indicating that there exists a very strong interaction between H atom and (100) surface. Similar results were obtained by Gong and co-authors [46].

Table 2. Calculated adsorption energy (E_{ads}), average distance between H atom and metal atom ($d_{\text{H-TM}}$) as well as average distance between H atom and the top layer ($d_{\text{H-Surf}}$) in slab model of Mo-doped Nb (100) surface for adsorbed hydrogen atoms at different sites indicated in Figure 4

Site	E_{ads} (eV)	$d_{\text{H-TM}}$ (Å)	$d_{\text{H-Surf}}$ (Å)
T2	-3.41	1.77	1.85
T1	-3.26	1.85	1.93
B2	-3.77	1.97	1.30
B1	-3.75	1.97	1.21
H2	-4.24	1.98	0.46
H1	-4.27	1.99	0.44

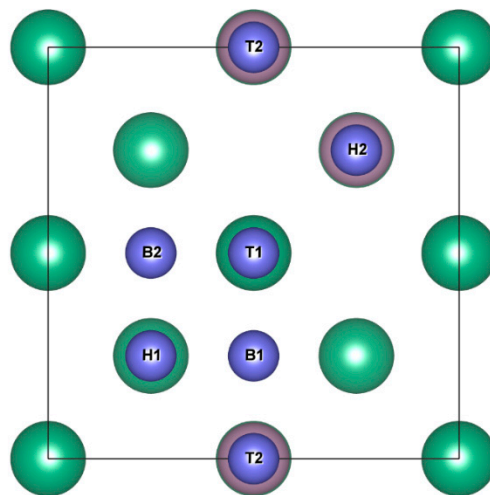


Figure 4. Schematic illustration of three possible locations of hydrogen atoms adsorbed onto Mo-doped Nb (100) surface: top site (T1, T2), bridge site (B1, B2), and hollow site (H1, H2).

3.3. Electronic Properties of Mo-doped Nb (100) Surface

To examine the interaction between atoms, we investigated the electronic properties of the Mo-doped Nb (100) surface. The calculated density of states (DOS) of H atom adsorbed at the bridge, hollow, and top sites are shown in Figure 5a–c, respectively. The Partial DOS (PDOS) peaks at about -30 eV with respect to the Fermi level are mainly contributed by Nb-*p* and Mo-*p* states for Mo-doped Nb (100) surface. The PDOS peaks near -5 eV are contributed by the H-*s* state. In the case of H1 model (Figure 5b), an obvious peak of Nb-*d* is observed at -5 eV, but it is absent in the case of B1 and T1 models, indicating that the hybridization between H-*s* and Nb-*d* states in B1 model is adjusted by Mo-doping.

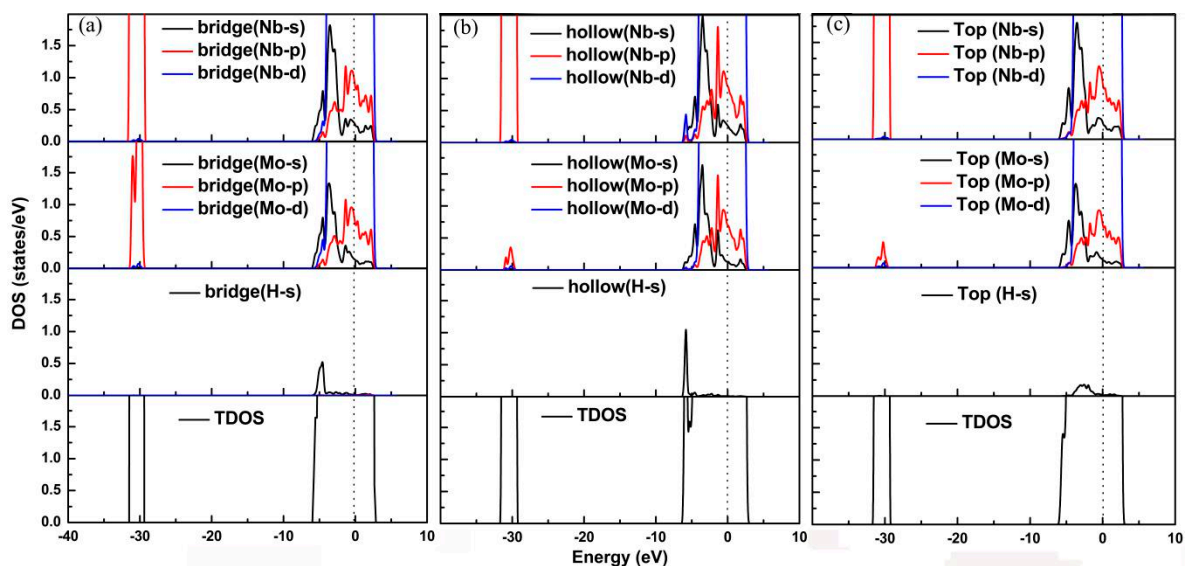


Figure 5. Calculated total and partial density of states of hydrogen atoms adsorbed onto Mo-doped Nb (100) surface at (a) B1 site, (b) H1 site, and (c) T1 site. The Fermi level is set to zero.

3.4. Diffusion of Hydrogen Atom into Mo-doped Nb (100) Subsurface

To further understand the behavior of H atoms diffusion, we investigate the subsequent H-diffusion process from the surface into the subsurface. The possible H-diffusion paths are H1→TIS and H1→OIS. We utilize CI-NEB method to determine the minimum energy and energy barrier for H-diffusion at both paths. The energy barrier of H1→TIS is 0.31 eV (Figure 6b), which is smaller than

the corresponding value (1.0 eV) of H1→OIS (Figure 6a), meaning that the H-diffusion path should mainly be H1→TIS. In addition, the energy barrier of H1→TIS of the pure Nb (100) surface is 0.82 eV (Figure 6c), indicating Mo-doping improves the performance of H-atom diffusion for Nb (100) surface.

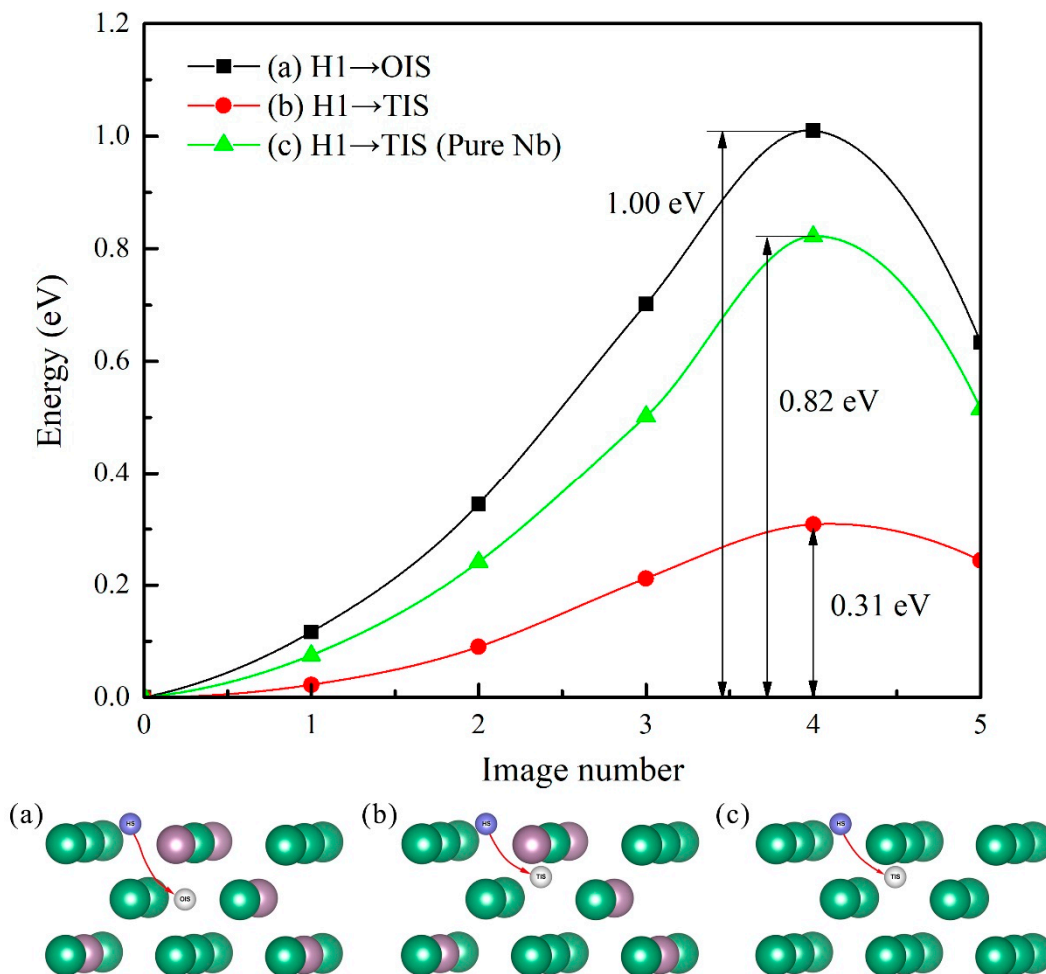


Figure 6. Energy barriers of H-atom diffusion in different path. (a) H1 to OIS in Mo-doped Nb (100) surface, (b) H1 to tetrahedral interstitial site in Mo-doped Nb (100) surface, and (c) HS to TIS in pure Nb (100) surface. Blue balls represent the starting position and white balls represent the finish position for H atoms.

4. Conclusions

The probable processes of atomic hydrogen adsorption, and diffusion behaviors on/into Mo-doped Nb (100) surface/subsurface are investigated using first-principles calculations in combination with empirical theory. Considering the above mentioned, we can come to the following conclusion:

(1) Comparing with the (111) surface, the (100) surface is more stable with smaller surface energy (2.75 J/m^2) for Mo-doped Nb.

(2) Among the three possible sites for H adsorption (BS, HS, and TS), H1 is most favorable due to its larger adsorption energy (-4.27 eV) and smaller average vertical distance between H atoms and the top layer of surface (0.44 \AA). The optimal H-diffusion path is H1→TIS for its low energy barrier of H-diffusion.

(3) The optimal H-diffusion path is H1→TIS. Furthermore, compared with pure Nb, Mo-doped Nb (100) surface offers a smaller energy barrier for H1→TIS path (0.31 eV), indicating that Mo-doping improves H adsorption and diffusion performance for Nb (100) surface.

Author Contributions: Z.W. (Zhongmin Wang) and C.H. conceived the work; Z.W. (Zhenzhen Wan) and Y.W. performed the calculations; Y.W. and D.W. wrote this manuscript; J.Q., Y.Z. and H.Z. made valuable comments on this manuscript.

Funding: This work was financially supported by the National Natural Science Foundation of China (51471055, 11464008, 51401060, and 51761007), the Natural Foundations of Guangxi Province (2014GXNSFGA118001 and 2016GXNSFGA380001), Guangxi Key Laboratory of Information Materials (131022-Z), and Guangxi Experiment Center of Information Science (YB1512).

Conflicts of Interest: The authors declare no conflict of interest.

References

1. Ding, L.; Wei, Y.; Li, L.; Zhang, T.; Wang, H.; Xue, J.; Wang, S.; Caro, J.; Gogotsi, Y. MXene molecular sieving membranes for highly efficient gas separation. *Nat. Commun.* **2018**, *9*, 155. [[CrossRef](#)] [[PubMed](#)]
2. Wang, Z.L.; Hao, X.F.; Jiang, Z.; Sun, X.P.; Xu, D.; Wang, J.; Zhong, H.; Meng, F.; Zhang, X. C and N hybrid coordination derived Co-C-N complex as a highly efficient electrocatalyst for hydrogen evolution reaction. *J. Am. Chem. Soc.* **2015**, *48*, 15070–15073. [[CrossRef](#)] [[PubMed](#)]
3. Li, F.; Zhong, B.; Xiao, H.; Ye, X.; Lu, L.; Guan, W.; Zhang, Y.; Wang, X.; Chen, C. Effect of degassing treatment on the deuterium permeability of Pd-Nb-Pd composite membranes during deuterium permeation. *Sep. Purif. Technol.* **2018**, *190*, 136–142. [[CrossRef](#)]
4. Ferrin, P.; Kandoia, S.; Nilekara, A.U.; Mavrikakisa, M. Hydrogen adsorption, absorption and diffusion on and in transition metal surfaces: A DFT study. *Surf. Sci.* **2012**, *606*, 679–689. [[CrossRef](#)]
5. Wang, J.W.; He, Y.H.; Gong, H.R. Various properties of Pd₃Ag/TiAl membranes from density functional theory. *J. Membr. Sci.* **2015**, *475*, 406–413. [[CrossRef](#)]
6. Wang, J.; Zhong, H.; Wang, Z.; Meng, F.L.; Zhang, X.B. Integrated three-dimensional carbon paper/carbon tubes/cobalt-sulfide sheets as an efficient electrode for overall water splitting. *ACS Nano* **2016**, *2*, 2342–2348. [[CrossRef](#)] [[PubMed](#)]
7. Zhong, H.; Wang, J.; Meng, F.; Zhang, X. In Situ Activating Ubiquitous Rust towards Low-Cost, Efficient, Free-Standing, and Recoverable Oxygen Evolution Electrodes. *Angew. Chem. Int. Ed.* **2016**, *34*, 9937–9941. [[CrossRef](#)]
8. Singh, M.E.; Rezac, P.H.; Pfromm, P. Hydrogenation of soybean oil using metal decorated integral-asymmetric polymer membranes: Effects of morphology and membrane properties. *J. Membr. Sci.* **2010**, *348*, 99–108. [[CrossRef](#)]
9. Singh, U.K.; Vannice, M.A. Kinetics of liquid-phase hydrogenation reactions over supported metal catalysts—A review. *Appl. Catal. A* **2001**, *213*, 1–24. [[CrossRef](#)]
10. Wang, J.; Li, K.; Zhong, H.; Xu, D.; Wang, Z.L.; Jiang, Z.; Wu, Z.; Zhang, X.B. Synergistic effect between metal-nitrogen-carbon sheets and NiO nanoparticles for enhanced electrochemical water-oxidation performance. *Angew. Chem. Int. Ed.* **2015**, *36*, 10530–10534. [[CrossRef](#)]
11. Zacher, A.H.; Olarte, M.V.; Santosa, D.M.; Elliott, D.C.; Jones, S.B. A review and perspective of recent bio-oil hydrotreating research. *Green Chem.* **2014**, *16*, 491–515. [[CrossRef](#)]
12. Carrette, L.; Friedrich, K.A.; Stimming, U. Fuel cells: Principles, types, fuels, and applications. *J. Chem. Phys.* **2000**, 1162–1193. [[CrossRef](#)]
13. Edwards, P.P.; Kuznetsov, V.L.; David, W.I.F.; Brandon, N.P. Hydrogen and fuel cells: towards a sustainable energy future. *Energy Policy* **2008**, *36*, 4356–4362. [[CrossRef](#)]
14. Kikuchi, E. Membrane reactor application to hydrogen production. *Catal. Today* **2000**, *56*, 97–101. [[CrossRef](#)]
15. Dong, W.; Ledentu, V.; Sautet, P.; Eichler, A.; Hafner, J. Hydrogen adsorption on palladium: A comparative theoretical study of different surfaces. *Surf. Sci.* **1998**, *411*, 123–136. [[CrossRef](#)]
16. Lauhon, L.J.; Ho, W. Direct observation of the quantum tunneling of single hydrogen atoms with a scanning tunneling microscope. *Phys. Rev. Lett.* **2000**, *85*, 4566. [[CrossRef](#)] [[PubMed](#)]
17. Gómez, E.D.V.; Amayaroncancio, S.; Avalle, L.B.; Linares, D.H.; Gimenez, M.C. DFT study of adsorption and diffusion of atomic hydrogen on metal surfaces. *Appl. Surf. Sci.* **2017**, *420*, 1–8. [[CrossRef](#)]
18. Mitsui, T.; Rose, M.K.; Fomin, E.; Ogletree, D.F.; Salmeron, M. Hydrogen adsorption and diffusion on Pd(111). *Surf. Sci.* **2003**, *540*, 5–11. [[CrossRef](#)]
19. Liu, Z.H.; Shang, J.X. Elastic properties of Nb-based alloys by using the density functional theory. *Chin. Phys. B* **2012**, *21*, 016202. [[CrossRef](#)]

20. Liu, G.; Besedin, S.; Irodova, A.; Liu, H.; Gao, G.; Eremets, M.; Wang, X.; Ma, Y. Nb-H system at high pressures and temperatures. *Phys. Rev. B* **2017**, *95*, 104110. [[CrossRef](#)]
21. Peterson, D.T.; Hull, A.B.; Loomis, B.A. Hydrogen embrittlement considerations in niobium-base alloys for application in the ITER divertor. *J. Nucl. Mater.* **2012**, *191–194*, 430–432.
22. Watanabe, N.; Yukawa, H.; Nambu, T.; Matsumoto, Y.; Zhang, G.X.; Morinaga, M. Alloying effects of Ru and W on the resistance to hydrogen embrittlement and hydrogen permeability of niobium. *J. Alloys Compd.* **2009**, *477*, 851–854. [[CrossRef](#)]
23. Zhang, G.X.; Yukawa, H.; Nambu, T.; Matsumoto, Y.; Morinaga, M. Alloying effects of Ru and W on hydrogen diffusivity during hydrogen permeation through Nb-based hydrogen permeable membranes. *Int. J. Hydrogen Energy* **2010**, *35*, 1245–1249. [[CrossRef](#)]
24. Yukawa, H.; Nambu, T.; Matsumoto, Y.; Watanabe, N.; Zhang, G.; Morinaga, M. Alloy design of Nb-based hydrogen permeable membrane with strong resistance to hydrogen embrittlement. *Mater. Trans.* **2008**, *49*, 2202–2207. [[CrossRef](#)]
25. Nambu, T.; Shimizu, K.; Matsumoto, Y.; Rong, R.; Watanabe, N.; Yukawa, H.; Morinaga, M.; Yasuda, I. Enhanced hydrogen embrittlement of Pd-coated niobium metal membrane detected by in situ small punch test under hydrogen permeation. *J. Alloys Compd.* **2007**, *446*, 588–592. [[CrossRef](#)]
26. Long, J.H.; Gong, H. Phase stability and mechanical properties of niobium dihydride. *Int. J. Hydrogen Energy* **2014**, *39*, 18989–18996. [[CrossRef](#)]
27. Slining, J.R.; Koss, D.A. Solid solution strengthening of high purity niobium alloys. *Metall. Trans.* **1973**, *4*, 1261–1264. [[CrossRef](#)]
28. Kozhakhmetov, S.; Sidorov, N.; Piven, V.; Sipatov, I.; Gabis, I.; Arinov, B. Alloys based on Group 5 metals for hydrogen purification membranes. *J. Alloys Compd.* **2015**, *645*, S36–S40. [[CrossRef](#)]
29. Xu, Z.J.; Wang, Z.M.; Tang, J.L.; Deng, J.Q.; Yao, Q.R.; Zhou, H.Y. Effects of Mo alloying on the structure and hydrogen-permeation properties of Nb metal. *J. Alloys Compd.* **2018**, *740*, 810–815. [[CrossRef](#)]
30. Wu, Y.; Wang, Z.M.; Wang, D.H.; Wan, Z.Z.; Zhong, Y.; Hu, C.H.; Zhou, H. Effects of Ni doping on various properties of NbH phases: A first-principles investigation. *Sci. Rep. UK* **2017**, *7*, 6535. [[CrossRef](#)]
31. Hu, Y.T.; Gong, H.; Chen, L. Fundamental effects of W alloying on various properties of NbH phases. *Int. J. Hydrogen Energy* **2015**, *40*, 12745–12749. [[CrossRef](#)]
32. Kong, X.S.; Wang, S.; Wu, X.; You, Y.W.; Liu, C.S.; Fang, Q.F.; Chen, J.L.; Luo, G.N. First-principles calculations of hydrogen solution and diffusion in tungsten: Temperature and defect-trapping effects. *Acta Mater.* **2015**, *84*, 426–435. [[CrossRef](#)]
33. Nagata, S.; Takahiro, K. Deuterium retention in tungsten and molybdenum. *J. Nucl. Mater.* **2000**, *283*, 1038–1042. [[CrossRef](#)]
34. Duan, C.; Liu, Y.L.; Zhou, H.B.; Zhang, Y.; Jin, S.; Lu, G.H.; Luo, G.N. First-principles study on dissolution and diffusion properties of hydrogen in molybdenum. *J. Nucl. Mater.* **2010**, *404*, 109–115. [[CrossRef](#)]
35. Wright, G.M.; Whyte, D.G.; Lipschultz, B. Measurement of hydrogenic retention and release in molybdenum with the DIONISOS experiment. *J. Nucl. Mater.* **2009**, *390–391*, 544–549. [[CrossRef](#)]
36. Kresse, G.; Hafner, J. Ab-initio molecular dynamics for liquid metals. *Phys. Rev. B* **1993**, *47*, 558–561. [[CrossRef](#)]
37. Kresse, G.; Furthmüller, J. Efficient iterative schemes for ab initio total-energy calculations using a plane-wave basis set. *Phys. Rev. B* **1996**, *54*, 11169–11186. [[CrossRef](#)]
38. Perdew, J.P.; Wang, Y. Accurate and simple analytic representation of the electron-gas correlation energy. *Phys. Rev. B* **1992**, *45*, 13244–13249. [[CrossRef](#)]
39. Blöchl, P.E. Projector augmented-wave method. *Phys. Rev. B* **1994**, *50*, 17953–17979. [[CrossRef](#)]
40. Perdew, J.P.; Burke, K.; Ernzerhof, M. Generalized gradient approximation made simple. *Phys. Rev. Lett.* **1996**, *77*, 3865. [[CrossRef](#)]
41. Henkelman, G.; Uberuaga, B.P.; Jonsson, H.A. Climbing image nudged elastic band method for finding saddle points and minimum energy paths. *J. Chem. Phys.* **2000**, *113*, 9901–9904. [[CrossRef](#)]
42. Lässer, R.; Bickmann, K. Phase diagram of the Nb-T system. *J. Nucl. Mater.* **1985**, *132*, 244–248. [[CrossRef](#)]
43. Baskes, M.I. Modified embedded-atom potentials for cubic materials and impurities. *Phys. Rev. B* **1992**, *46*, 2727. [[CrossRef](#)]
44. Strayer, R.W.; Mackie, W.; Swanson, L.W. Work function measurements by the field emission retarding potential method. *Surf. Sci.* **1973**, *34*, 225–248. [[CrossRef](#)]

45. Michaelson, H.B. The work function of the elements and its periodicity. *J. Chem. Phys.* **1977**, *48*, 4729–4733. [[CrossRef](#)]
46. Gong, L.; Su, Q.; Deng, H.; Xiao, S.; Hu, W. The stability and diffusion properties of foreign impurity atoms on the surface and in the bulk of vanadium: A first-principles study. *Comput. Mater. Sci.* **2014**, *81*, 191–198. [[CrossRef](#)]



© 2018 by the authors. Licensee MDPI, Basel, Switzerland. This article is an open access article distributed under the terms and conditions of the Creative Commons Attribution (CC BY) license (<http://creativecommons.org/licenses/by/4.0/>).